https://doi.org/10.5194/essd-2025-760
Preprint. Discussion started: 19 February 2026

Open Access Earth System Science Data Discussions

The first decadal-scale ground-based microwave radiometer dataset in China: Brightness temperature and thermodynamic profiles from Xianghe (2013–2022)

Yueyuan Gong[1,2], Wenying He[1,2], Disong Fu[3], Xiang'ao Xia[1,2], Hongrong Shi[3], Weidong Nan[4], Pucai Wang[1,2], and Hongbin Chen[1,2]

[1]Laboratory of Middle Atmosphere and Global Environment Observation (LAGEO), Institute of Atmospheric Physics, Chinese Academy of Sciences, Beijing 100029, China
[2]College of Earth and Planetary Sciences, University of Chinese Academy of Sciences, Beijing, China
[3]State Key Laboratory of Atmospheric Environment and Extreme Meteorology, Institute of Atmospheric Physics, Chinese Academy of Sciences, Beijing 100029, China
[4]Xianghe Observatory of Whole Atmosphere, Institute of Atmospheric Physics, Chinese Academy of Sciences, Xianghe 065400, China

Correspondence to: Wenying He (hwy@mail.iap.ac.cn) and Disong Fu (fudisong@mail.iap.ac.cn)

Abstract. Ground-based microwave radiometers (MWRs) are indispensable instruments for the continuous observation of atmospheric temperature and humidity profiles. The reliability of brightness temperature (TB) measurements and the accuracy of retrieved atmospheric profiles are fundamental to their effective use in both research and operational applications. In this study, we present a long-term dataset of multi-channel microwave brightness temperature observations and corresponding retrieved atmospheric profiles derived from the RPG-HATPRO MWR deployed at the Xianghe Integrated Observatory (XH) in Hebei Province, China, covering the period 2013–2022. Minute-level TB observations over the 10-year period were integrated with collocated infrared cloud detection data to establish a comprehensive dataset featuring a detailed weather-type classification. The quality of the observed TBs was carefully evaluated using a radiative transfer model. The results demonstrate excellent agreement between simulated and observed multi-channel TBs, with correlation coefficients typically exceeding 0.96 and mean biases within 1 K, confirming the stable and reliable performance of the XH MWR throughout the entire observation period. Based on the quality-controlled TBs, two retrieval schemes for atmospheric temperature and humidity profiles were developed using collocated radiosonde observations and ERA5 reanalysis data. For clear-sky conditions, an optimal estimation (OE)-based retrieval model was employed, whereas a deep neural network (DNN)-based model was designed for cloudy-sky retrievals. Validation against radiosonde measurements shows that both retrieval schemes achieved substantially improved accuracy up to 35 % for temperature and 25 % for humidity profiles by compared with the MWR's self-developed products. Combining the two retrieval models with the 10-year quality-controlled TB dataset, we constructed a comprehensive data record characterized by decadal-scale, high temporal resolution (1~10 min), and integrated MWR observations and profiles dataset. Based on the long-term dataset, it reveals a weak but consistent near-surface warming trend across 100–1000 m. They also capture the frequent surface-based inversions, occurred from 6% in summer to 68% in winter. Critically, SBI occurrence increases with $PM_{2.5}$ levels, reaching >60% under severe pollution (>250 $\mu g\,m^{-3}$). Those applications demonstrate the dataset's value for boundary layer studies, climate trend analysis, and air quality forecasting.

https://doi.org/10.5194/essd-2025-760
Preprint. Discussion started: 19 February 2026

Open Access Earth System Science Data Discussions

1 Introduction

The vertical distribution of atmospheric temperature and humidity is a key parameter for understanding the thermodynamic and dynamic processes of the atmosphere, particularly within the planetary boundary layer and the troposphere, where weather systems frequently occur and are strongly influenced by human activities. Traditionally, atmospheric temperature and humidity profiles are obtained through radiosonde measurements carried by weather balloons, which provide highly accurate and reliable data and are widely regarded as reference standards for validating other atmospheric profile products (He et al., 2019; Trent et al., 2023). However, the routine radiosonde launches, typically conducted twice daily, suffer from low temporal resolution and high operational cost, making them unsuitable for monitoring short-lived mesoscale weather systems. The ground-based microwave radiometer (MWR) is a passive remote sensing instrument that measures the atmospheric thermal emission affected by water vapor and oxygen molecules, allowing for the retrieval of temperature and humidity profiles, as well as the integrated water vapor (IWV) and liquid water path (LWP) along the line of sight (Turner et al., 2007; Xu, 2024). MWRs have become mature and robust instruments capable of unattended, all-weather operation, providing high temporal resolution (e.g., minute-level) atmospheric profiles that greatly complement radiosonde observations (Löhnert and Maier, 2012) and offer valuable input for nowcasting and numerical weather prediction systems (Rüfenacht et al., 2021).

Compared with satellite-based retrievals, which are limited by surface heterogeneity and reduced sensitivity within the boundary layer, MWRs offer distinct advantages through their multi-frequency measurements and upward-looking perspective, enabling continuous and dynamic monitoring of boundary-layer meteorological variables (Cimini et al., 2020; Madhulatha et al., 2013). These observations have proven particularly useful for diagnosing the vertical structure of severe air pollution events and investigating the mechanisms of haze formation (Huang et al., 2013; Temimi et al., 2020; Zhang et al., 2024). Moreover, MWRs are highly sensitive to variations in lower- and mid-tropospheric thermodynamic structures and are therefore widely applied in assessing atmospheric stability, cloud microphysical evolution, air pollution, and hazardous weather events (Cimini et al., 2015; Liu et al., 2025; Madhulatha et al., 2013; Zhou et al., 2024).

In general, MWR observations provide Level 1 (LV1) data, which record the measured brightness temperature (TB) representing the intensity of atmospheric microwave radiation. Based on multi-channel TB observations, various atmospheric parameters—including temperature and humidity profiles, IWV, and LWP—can be retrieved to produce Level 2 (LV2) products. The accuracy of LV2 retrievals is inherently dependent on the quality of LV1 TB measurements; therefore, a rigorous assessment of LV1 data quality is an essential prerequisite for the reliable application of MWR observations (Zou et al., 2021). The radiative transfer model (RTM), which quantitatively describes the propagation of electromagnetic radiation through the atmosphere via the radiative transfer equation, serves as a physical link between observed and simulated radiances. RTMs are widely employed for evaluating the quality of both satellite-based and ground-based radiometric observations (De Angelis et al., 2017; Hou et al., 2019). Because RTMs are independent of instrument calibration and operational conditions, the simulated TBs they generate provide an objective and physically consistent benchmark for validating MWR LV1 observations (He et al.,

https://doi.org/10.5194/essd-2025-760
Preprint. Discussion started: 19 February 2026

2021; Navas-Guzmán et al., 2016). Once the reliability of the observed TBs is established, multi-channel retrieval algorithms can be applied to derive LV2 atmospheric parameters with improved confidence.

Current MWR retrieval algorithms can generally be classified into two categories: statistical methods and physical methods. Statistical approaches, such as multivariate regression and neural network algorithms, rely on historical radiosonde datasets to establish empirical relationships between observed TBs and atmospheric parameters (Zhao et al., 2018; Zhu et al., 2022). These methods are computationally efficient and suitable for real-time applications but depend heavily on the completeness and representativeness of the training dataset, requiring regional adjustments for optimal performance. Physical retrieval methods, on the other hand, explicitly incorporate the radiative transfer equation and prior information of atmospheric state variables to estimate the most probable atmospheric profile using optimal estimation theory (Hewison, 2007; Maahn et al., 2020; Martinet et al., 2015). While less dependent on large training datasets, physical methods are computationally intensive, especially under cloudy or precipitating conditions (Yan et al., 2020).

With the increasing deployment of MWRs, numerous studies have focused on data quality control and retrieval algorithm development. However, most efforts have concentrated on specific events or short-term datasets, typically employing a single retrieval model for all conditions, which limits their ability to account for the radiative characteristics under diverse weather situations. To address these limitations, this study utilizes ten years (2013–2022) of TB observations from the RPG-HATPRO MWR at the Xianghe Atmospheric Observatory operated by the Institute of Atmospheric Physics, Chinese Academy of Sciences ((hereafter referred to as XH). By integrating collocated infrared cloud detection data, we establish a multi-channel MWR TB dataset with a weather-type classification system. The data quality is further evaluated using an RTM combined with atmospheric temperature and humidity profiles from the ERA5 reanalysis dataset, and long-term variations in TBs under clear-sky and different cloud conditions are analyzed. Based on the quality-controlled multi-channel TBs and weather-type flags, together with radiosonde and ERA5 reanalysis profiles, two retrieval schemes are developed for different weather scenarios: an optimal estimation (OE) retrieval model for clear-sky conditions and a deep neural network (DNN) retrieval model for cloudy conditions. Both models are validated against radiosonde observations. Using these two schemes, the 10-year quality-controlled dataset is processed to generate retrieved temperature and humidity profiles, and the temporal evolution of near-surface thermodynamic structures over XH is analyzed.

The structure of this paper is as follows: Section 1 presents the introduction and research background; Section 2 describes the observational instruments and datasets; Section 3 details the construction of the 10-year MWR TB dataset; Section 4 introduces the retrieval models and their validation; and Section 5 summarizes the main findings.

2 Observation instruments and data

An RPG-HATPRO ground-based MWR consisting of 14 frequency channels is deployed at XH (39.75° N, 117.00° E). The first seven channels (22.24–31.40 GHz) are centered on the water vapor absorption line and are used to retrieve atmospheric

https://doi.org/10.5194/essd-2025-760
Preprint. Discussion started: 19 February 2026

humidity parameters, including absolute and relative humidity, IWV, and LWP. The remaining seven channels (51.26–58.00 GHz) are located around the oxygen absorption line and provide information on atmospheric temperature profiles.

Additionally, several auxiliary instruments are installed on the MWR, including a rain sensor, an infrared (IR) radiometer, and an automatic weather station (AWS). The rain sensor continuously records precipitation signals (*Rainflag*), while the IR radiometer, operating in the 9.2–10.6 μm spectral range, measures zenith-direction infrared brightness temperatures (IRTs) to estimate cloud base height (CBH). The AWS monitors near-surface meteorological variables such as air temperature, pressure, and humidity, providing essential background information for atmospheric observations.

The RPG system also includes a self-developed inversion module that produces Level 2 (LV2) temperature and humidity profiles up to 10 km altitude (Bedoya-Velásquez et al., 2019). The vertical structure consists of 39 layers, with 25 layers below 2 km (vertical resolution 10–200 m) and additional layers up to 10 km (resolution 200–2000 m). To ensure long-term accuracy, the instrument undergoes absolute calibration using liquid nitrogen every six months, and the microwave window is cleaned with purified water approximately every three months to prevent contamination.

In this study, we primarily used the multi-channel LV1 TB data recorded at second-level temporal resolution during 2013–2022, along with collocated IRTs and rain detection data for identifying cloudy and precipitating conditions. Evaluation of LV1 TB quality using a radiative transfer model required atmospheric profiles, which were obtained from two sources: (1) the Beijing radiosonde station (No. 54511), located at the Beijing Meteorological Observation Center, providing twice-daily balloon soundings up to ~30 km (Lai et al., 2024); and (2) the ERA5 reanalysis dataset from the European Centre for Medium-Range Weather Forecasts (ECMWF), offering hourly profiles at 0.25° × 0.25° spatial resolution (Hersbach et al., 2020). ERA5 profiles were used to provide continuous atmospheric input for assessing MWR performance via the radiative transfer model, whereas radiosonde profiles served as “ground truth” for validating the retrieval algorithms developed in this study.

In addition, auxiliary observational datasets are used to evaluate the cloud detection derived from the MWR retrievals. Specifically, ground-based $PM_{2.5}$ (particulate matter with aerodynamic diameters $\leqslant$ 2.5 μm) concentration measurements from the same site during 2018-2019 are incorporated to investigate the potential influence of aerosol pollution on thermodynamic profiles (Xin et al., 2015).

3 Construction of a 10-year ground-based MWR TB Dataset

Ground-based MWRs retrieve atmospheric temperature and humidity profiles from multi-channel TB observations. Consequently, the accuracy of these retrieved profiles depends critically on the quality of the TB observations. When deployed outdoors for long-term monitoring, MWRs are influenced not only by varying meteorological conditions but also by occasional instrumental anomalies, such as electromagnetic interference, power instability, or communication failures (Fu and Tan, 2017; Zhu et al., 2022). Therefore, LV1 TB observations require rigorous quality control (QC) prior to their use in retrieval or analysis applications.

https://doi.org/10.5194/essd-2025-760
Preprint. Discussion started: 19 February 2026

Open Access Earth System Science Data Discussions

3.1 Quality control and classification of TB observations

For the multi-channel TB observations collected by the XH ground-based MWR, a comprehensive TB quality control and weather classification procedure was developed. The workflow includes singular value checking, precipitation screening, and clear-sky and cloudy-sky identification, as illustrated in Fig. 1.

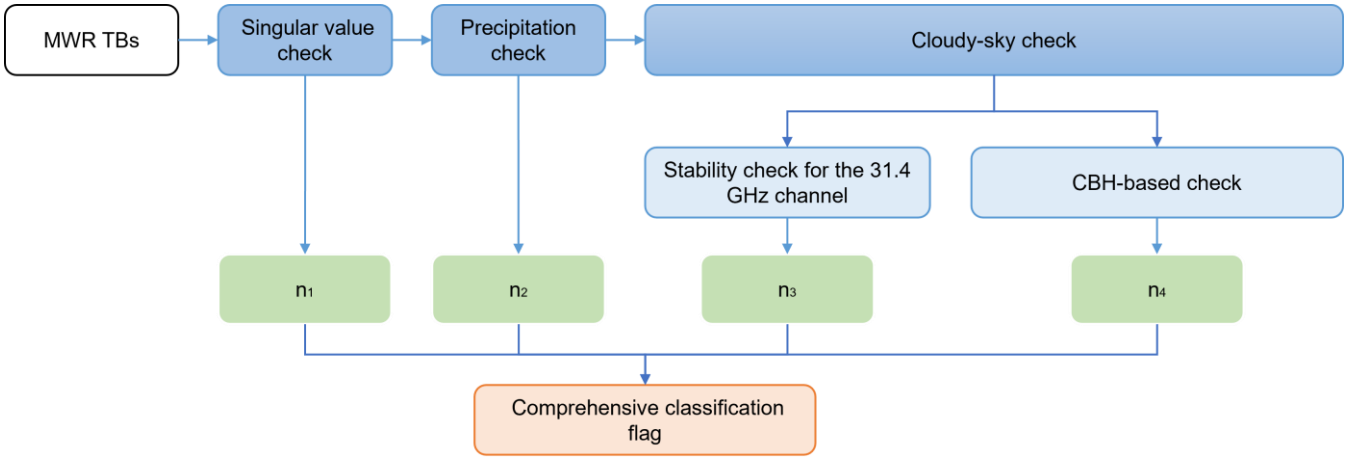

Figure 1: Flowchart of TB quality control and weather identification and classification.

3.1.1 Singular value check

Long-term TB observations are subjected to outlier detection and initial QC. A quality identifier, denoted by the integer n_1, is assigned to each record (see Table 1). The judgment criterion is based on the mean (μ) and standard deviation (σ) of TB within each season: if the TB at time n, denoted TB(n), satisfies $|TB(n) - \mu| \leq 3\sigma$, the observation is considered valid; otherwise, it is flagged as anomalous.

Because MWRs operate continuously in outdoor environments, the radome can accumulate dust, moisture, or other contaminants, which may degrade measurement sensitivity and accuracy. Regular cleaning of the radome with purified water under clear-sky conditions is necessary, but this procedure often induces temporary abnormal increases in TB, resembling precipitation signals. Following cleaning, TB values generally return to normal within 1–2 hours, and up to 4 hours in winter. Based on maintenance logs, TB observations recorded within 4 hours after radome cleaning are flagged as abnormal (n_1 = 1 in Table 1).

Table 1. Multi-Identifier for TB observations and the meanings of its values

Identifier	Value	Checking Condition	Meaning
n_1	0	$\|TB(n) - \mu\| \leq 3\sigma$ and not within cleaning window	Normal
	1	Within 4 hours after cleaning	Abnormal
	2	$\|TB(n) - \mu\| > 3\sigma$	Abnormal
n_2	0	*Rainflag* = 0	No precipitation

https://doi.org/10.5194/essd-2025-760
Preprint. Discussion started: 19 February 2026

Open Access Earth System Science Data Discussions

Identifier	Value	Checking Condition	Meaning
	1	*Rainflag* = 1	Precipitation
n_3	0	$\sigma_c \leq a + b \cdot \mathrm{IWV}$	Clear-sky
	1	$\sigma_c > a + b \cdot \mathrm{IWV}$	Cloudy
n_4	0	$\mathrm{IRT} \leq \mathrm{IRT}_{\mathrm{threshold}}$	Clear-sky
	1	$\mathrm{IRT} > \mathrm{IRT}_{\mathrm{threshold}}$	Cloudy
nflag	0	n_1=0, n_2=0, n_3=0, n_4=0	Clear-sky
	1	n_1=0, n_2=0, (n_3=1 or n_4=1)	Cloudy
	2	n_1=0, n_2=1	Precipitation
	3	n_1=1	Other/uncertain

3.1.2 Precipitation check

During precipitation events, residual water layers on the radome may cause large uncertainties in TB observations, directly affecting retrieval accuracy (Wei et al., 2021). Therefore, after removing anomalous values via the singular value check, precipitation-related data are further screened. The LV1 TB data from the RPG-HATPRO MWR include a *Rainflag* provided by a collocated precipitation sensor, indicating precipitation conditions: *Rainflag* = 0 denotes no precipitation, and *Rainflag* = 1 denotes precipitation. Accordingly, precipitation conditions are represented by identifier n_2, as defined in Table 1.

3.1.3 Cloudy-sky check

Two complementary methods were used to identify cloudy conditions. The first method exploits the high sensitivity of the 31.4 GHz water vapor channel (CH7) to liquid water in clouds, analyzing TB fluctuations to detect cloud presence. The second approach incorporates CBH information derived from co-located infrared radiometer measurements to refine the classification of cloud and clear periods.

a) Stability check for the 31.4 GHz channel

Given that the high-frequency water vapor channel CH7 (31.4 GHz) is sensitive to liquid water in clouds, its observed TB exhibits noticeable fluctuations when clouds are present. Therefore, the stability of CH7 observations over a specific time period—quantified by the standard deviation within a given time window—can serve as a reference indicator for the presence of clouds during that period.

Following the approach of Turner et al., (2007), this study uses a 30-minute time window to calculate the standard deviation of CH7 observed TB, denoted as σ_c. The stability of the 31.4 GHz channel is then assessed by comparing σ_c against a threshold defined as $a + b \cdot \mathrm{IWV}$, where IWV represents the total column water vapor, and the parameters are set as a = 0.15 K and b =

https://doi.org/10.5194/essd-2025-760
Preprint. Discussion started: 19 February 2026

0.06 K/cm. Based on this method for identifying cloudy conditions, the observed TB data are classified using the identifier n_3: $n_3 = 0$ for clear sky and $n_3 = 1$ for cloudy sky.

b) CBH-based check

To further improve cloud detection accuracy, the CH7-based method is complemented with cloud-base height (CBH) information obtained from a zenith-view infrared radiometer (IRT). The CBH value itself provides a physical constraint for identifying clear-sky periods. In this study, cases where the IRT reports no detectable cloud base are treated as clear-sky conditions ($n_4 = 0$). Conversely, cases with CBH higher than approximately 6–8 km are typical cirrus altitudes and lower than about 3 km is generally associated with low and mid-level clouds and is classified as cloudy ($n_4 = 1$).

3.1.4 Comprehensive classification flag

To facilitate the correct use of ground-based microwave radiometer observations, a comprehensive classification identifier, *nflag*, was established by integrating all the aforementioned classification flags. Its values and corresponding meanings are listed in Table 1, where "Other" indicates data with additional quality uncertainties and is not recommended for use.

Thus, based on TB observations obtained from the ground-based microwave radiometer during 2013–2022, the raw data were first subjected to an initial quality screening to remove outliers. Weather conditions—including precipitation, clear sky, and cloudy sky—were then identified and classified using multiple criteria. The final result is a nearly ten-year, high-temporal-resolution (~1 min) multichannel TB long-term dataset, providing a reliable foundation for analyzing observational TB characteristics under different weather conditions, performing radiative simulations, and conducting atmospheric temperature and humidity profile retrievals.

3.2 Evaluation of observed brightness temperature quality using a radiative transfer model

Assessing the quality of MWR TBs using a radiative transfer model is a scientifically sound and efficient approach. By comparing the theoretical TB simulated from the radiative transfer model with the actual measurements, abnormal values and potential systematic biases in the observations can be effectively identified, thereby enabling a comprehensive evaluation of the observation quality and instrument performance (De Angelis et al., 2017).

Typically, only clear-sky samples are selected for such simulations, as the atmospheric state under clear-sky conditions is relatively stable and free from cloud and precipitation interference. In this case, the radiative transfer process is primarily influenced by water vapor and oxygen absorption, resulting in the lowest simulation uncertainty. Therefore, if significant discrepancies still exist between the observed and simulated TB after removing the effects of precipitation and clouds, these differences likely indicate instrumental malfunctions or observational errors.

Based on the TB dataset constructed in Section 3.1, which includes weather classification information, clear-sky TB data were selected and evaluated using a radiative transfer model. By systematically comparing the consistency between observed and simulated TB, a precise quality assessment of the MWR observations was achieved.

https://doi.org/10.5194/essd-2025-760
Preprint. Discussion started: 19 February 2026

3.2.1 Radiative transfer model and evaluation method

To assess the quality of observed TB data, the MWRT (Microwave Radiative Transfer) model (Liu, 1998) was employed. MWRT is based on the four-stream discrete ordinate method to solve the radiative transfer equation, achieving high computational accuracy while maintaining good efficiency. Previous studies have demonstrated that MWRT outperforms other commonly used radiative transfer models in simulating ground-based MWR observations (He et al., 2021; Zou et al., 2021).

To simulate MWR-observed TBs, MWRT requires input atmospheric profiles, including pressure, temperature, and humidity. As no local radiosonde data are available at XH and the nearest sounding station provides only two profiles per day (morning and evening), hourly ERA5 reanalysis data with a spatial resolution of 0.25° were used to provide the atmospheric state fields. The quality of MWR TB observations was then quantitatively assessed by comparing simulated and measured TBs using three statistical indicators: mean bias (MB), correlation coefficient (R), and standard deviation (STD). These metrics respectively characterize bias, correlation, and dispersion, thereby providing a comprehensive evaluation of observation accuracy and reliability.

3.2.2 Quality assessment of observed brightness temperature

Given the accuracy of radiative transfer simulations under clear-sky conditions, the TBs observed by the ground-based microwave radiometer are expected to be consistent with simulated TBs. In the comparison study, a spatiotemporal synchronization approach was applied: the quality-controlled observational dataset was matched with the forward-modeled TBs within a close temporal window, and data with anomalous deviations were removed using the 3σ criterion based on the Root Mean Square Error (RMSE).

Figure 2 presents scatter plots comparing observed and simulated TBs under clear-sky conditions during 2013-2022. Statistics from ~28,000 matched samples show that R values between simulated and observed TBs are close to 1.0 for most channels, with data points concentrated along the 1:1 line, indicating strong agreement. This result confirms both the physical reliability of the observed TBs and the long-term stability of the MWR instrument. Among the O_2 channels, the low-frequency oxygen channel at 51.26 GHz (CH8) shows a slightly lower correlation (~0.98) and the largest mean bias (~1.51K), which can be attributed to its sensitivity to lower- and mid-tropospheric water vapor as well as residual uncertainties in oxygen absorption parameterizations within radiative transfer models (Zou et al., 2021).

https://doi.org/10.5194/essd-2025-760
Preprint. Discussion started: 19 February 2026

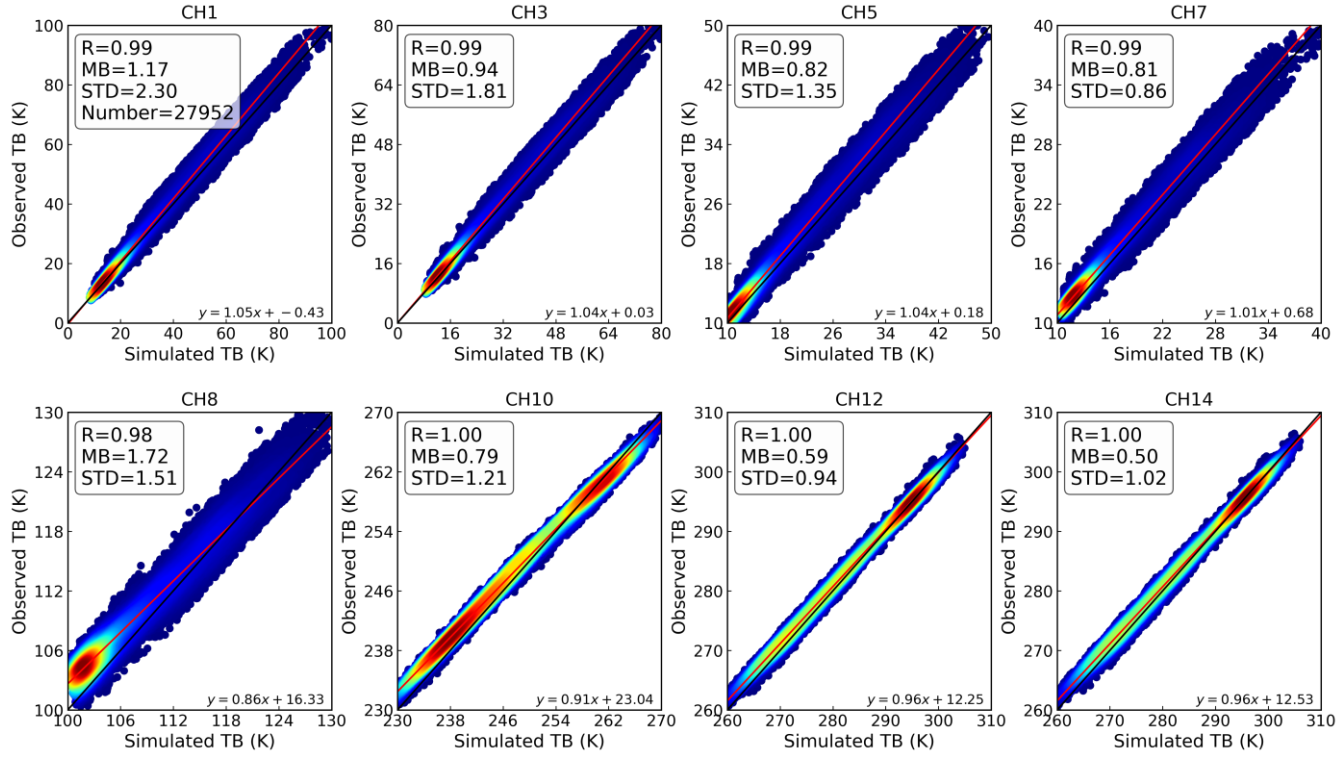

Figure 2: Scatter plots of multi-channel observed and simulated TB during 2013-2022.

To systematically evaluate the long-term performance of the ground-based MWR, statistical analyses of R, MB, and STD were conducted for multi-channel observed and simulated TBs over the 10-year period (2013–2022). As shown in Fig. 3, except for 2013—when limited observation samples slightly reduced correlations in the water vapor channels—the correlation coefficients for all channels remain highly consistent across the remaining years. The water vapor channels (CH1–CH7) and temperature channels (CH10–CH14) both show R > 0.98, indicating excellent consistency between simulated and observed TBs. For the low-frequency oxygen channels (CH8 and CH9), correlation coefficients are slightly reduced, consistent with the results in Fig. 2, likely due to channel sensitivity to water vapor and limitations in the radiative transfer model. In terms of MB, except for 2013, the water vapor channels show a decreasing MB with increasing frequency. The largest MB is observed for CH8 (51.26 GHz), while the high-frequency oxygen channels (CH10–CH14) remain relatively stable. For STD, CH1 shows the largest values among the water vapor channels, which decrease progressively with frequency, whereas the high-frequency oxygen channels (CH10–CH14) maintain small and stable STD values.

Overall, the 2013–2022 evaluation of the MWR TB data using MWRT simulations confirms the instrument's long-term stability and the reliability of its measurements. Based on this foundation, a multi-parameter dataset was constructed by integrating the quality-controlled, weather-classified, minute-resolution, multi-channel TB observations with corresponding IRTs, CBHs, and MWR-derived IWV and LWP.

https://doi.org/10.5194/essd-2025-760
Preprint. Discussion started: 19 February 2026

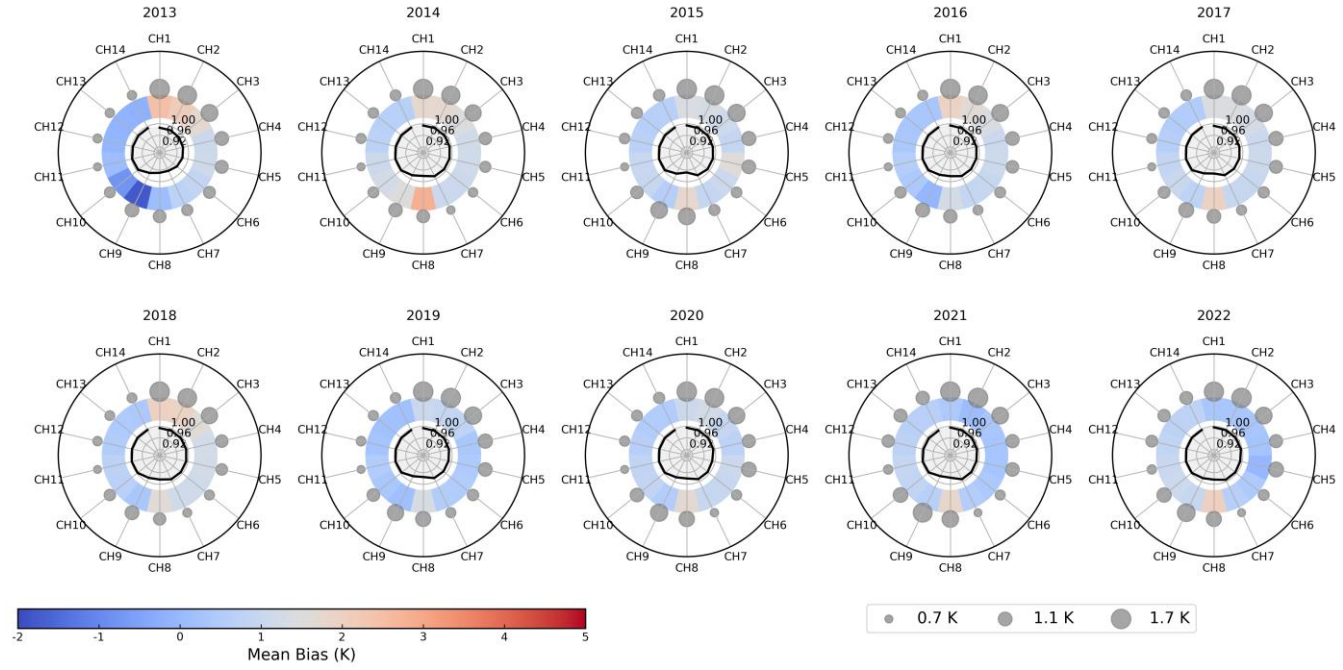

Figure 3: Ten-year (2013-2022) polar summary of the agreement between observed and ERA5-simulated brightness temperatures for all 14 channels. Each subplot shows one year, with the inner black solid curve representing the R, the middle colour shaded ring indicating the mean bias, and the circle marker sizes in the outer ring representing the standard deviation of differences. The bottom horizontal colorbar denotes the bias scale, and the adjacent legend explains the marker sizes for standard deviation

3.3 Retrieval and evaluation of atmospheric temperature and humidity profiles

Based on the dataset constructed in Section 3.1, together with radiosonde and ERA5 reanalysis data providing vertical atmospheric information, retrieval algorithms for atmospheric temperature and humidity profiles were developed under different weather conditions.

Currently, retrieval algorithms can generally be divided into two categories: statistical and physical methods. Statistical retrievals establish empirical relationships between atmospheric state parameters and multi-channel microwave TBs. These approaches are computationally efficient but sensitive to the quality and representativeness of the training samples. In contrast, physical retrievals are based on radiative transfer theory and estimate atmospheric parameters through inverse modeling. They are more physically consistent but computationally intensive and often require accurate prior knowledge of the atmosphere. Considering that radiative transfer simulations are more reliable under clear-sky conditions, this study adopts the OE method—a physically based inversion technique—for clear-sky retrievals. Under cloudy conditions, where complex scattering and emission processes increase model uncertainty, a DNN approach was employed as a statistical retrieval method.

https://doi.org/10.5194/essd-2025-760
Preprint. Discussion started: 19 February 2026

3.3.1 Optimal Estimation (OE) method

The OE method is grounded in Bayesian theory (Rodgers, 2000), which can be expressed as:

$$P(x|y) = \frac{P(y|x)P(x)}{P(y)}, \quad (1)$$

where $P(y \mid x)$ represents the likelihood function describing uncertainties in the measurement process and forward model, $P(x)$ defines the prior probability distribution of the atmospheric state, and $P(y)$ is a normalization factor ensuring that the posterior probability integrates to one. The posterior probability $P(x \mid y)$ thus quantifies the likelihood of a given atmospheric state x given the observation y.

In this study, the prior dataset for the OE retrieval was constructed using radiosonde profiles from the Beijing station during 2016–2019. The station, located approximately 55 km from Xianghe (XH), provides vertical profiles of atmospheric pressure, temperature, and humidity twice daily (around 08:00 and 20:00 local time). These radiosonde observations were used to characterize the climatological variability of the atmospheric state and to construct the prior covariance matrix required in the OE framework. They also serve as an independent reference for evaluating the retrieval accuracy.

3.3.2 Deep Neural Network (DNN) method

DNNs have been widely applied in remote sensing retrievals. Common neural network architectures include the backpropagation (BP) network, convolutional neural network (CNN), and recurrent neural network (RNN) (Guo et al., 2021; Malmgren-Hansen et al., 2019; Zhao et al., 2018). Among these, the BP neural network is well suited for nonlinear regression problems, as it can approximate complex functions without explicitly constructing a physical forward model. While a standard BP network typically includes only a single hidden layer, a DNN extends this structure by stacking multiple hidden layers, enhancing feature extraction and nonlinear representation capabilities.

A typical DNN consists of an input layer, multiple hidden layers, and an output layer. Each neuron in the input layer represents a feature (in this case, one microwave channel), and neurons in the hidden layers apply weighted transformations followed by nonlinear activation functions. The network is trained via forward and backward propagation, and regularization techniques such as Dropout are employed to prevent overfitting.

In this study, a DNN-based retrieval model was developed for MWR profile retrieval (Fig. 4). The input comprises 14-channel TBs, and the output corresponds to temperature and humidity profiles from 0–10 km. The training dataset was constructed using temporally matched MWR TB observations from 2019 and corresponding ERA5 temperature and humidity profiles as targets. After removing missing values, all input features were normalized to ensure consistent data scaling. The dataset was randomly divided into training, validation, and test sets in a 6:2:2 ratio to maintain both randomness and reproducibility. The DNN architecture consists of three hidden layers, each using the LeakyReLU activation function and batch normalization to enhance nonlinearity and accelerate convergence. Dropout regularization was applied to each hidden layer to prevent overfitting, while a linear activation was used in the output layer for regression. The model was optimized

https://doi.org/10.5194/essd-2025-760
Preprint. Discussion started: 19 February 2026

using the mean squared error (MSE) loss function, with EarlyStopping and ReduceLROnPlateau strategies applied—training was terminated if no improvement was observed for 15 consecutive epochs, and the learning rate was halved if no improvement occurred for 5 epochs.

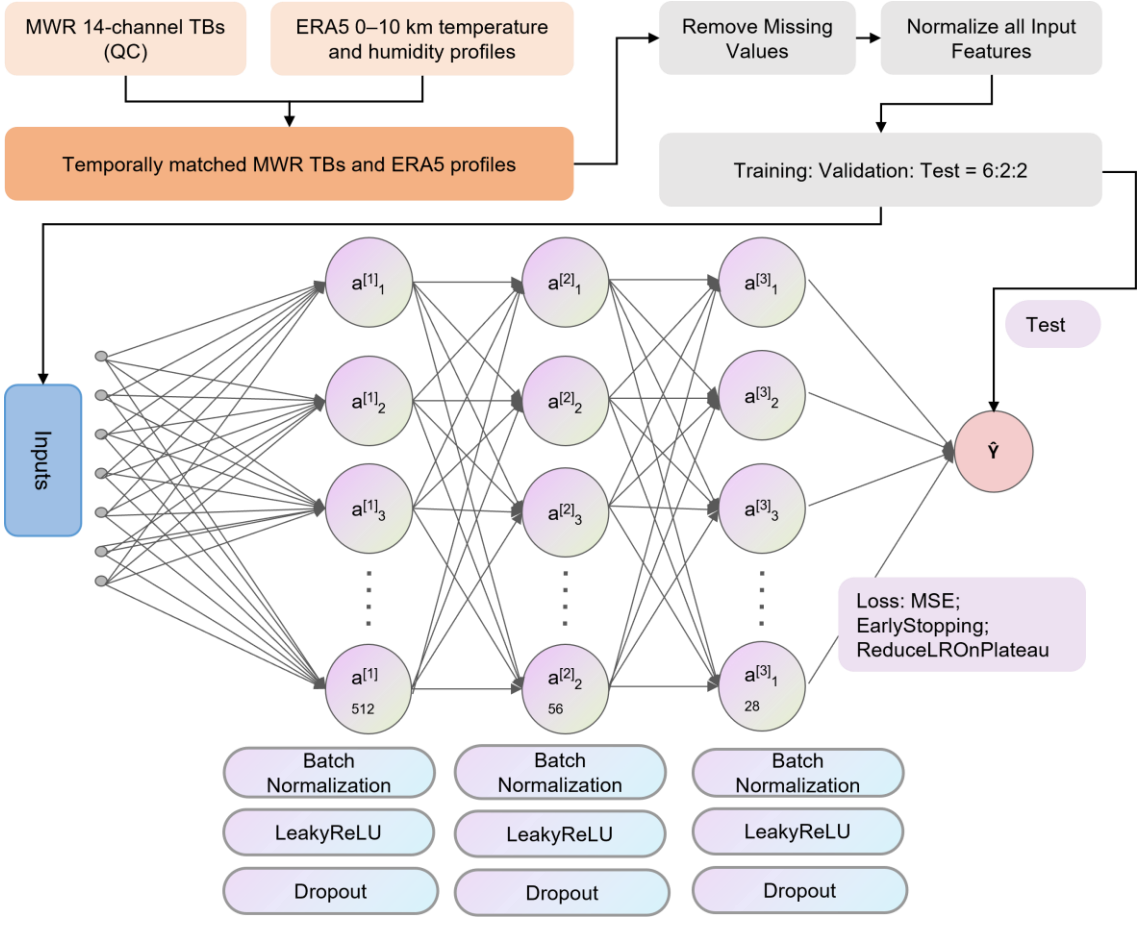

Figure 4: Flowchart of DNN model construction.

3.3.3 Quality assessment of retrievals

To quantitatively evaluate retrieval performance, radiosonde-measured temperature and humidity profiles from 2020 were used as the reference "truth." Both the OE- and DNN-based retrievals, derived from 2020 MWR TB observations, were assessed against these independent profiles. Three statistical metrics were employed: MB, R, and STD. To further quantify improvements relative to the MWR LV2 operational product, an accuracy improvement rate (Zhang et al., 2020) was introduced, calculated as:

$$k = \frac{(s_m + \bar{x}_m) - (s_r + \bar{x}_r)}{(s_m + \bar{x}_m)}, \quad (2)$$

https://doi.org/10.5194/essd-2025-760
Preprint. Discussion started: 19 February 2026

Open Access Earth System Science Data Discussions

where k is the accuracy improvement rate, $\bar{x}_m$ is the mean bias of the LV2 product, calculated as $\bar{x}_m = \frac{1}{n}\sum_{i=1}^{n} x_{mi}$, and $\bar{x}_r$ is the mean bias of the new model retrieval, $\bar{x}_r = \frac{1}{n}\sum_{i=1}^{n} x_{ri}$. The standard deviations are

$$s_m = \sqrt{\frac{1}{n}\sum_{i=1}^{n}(x_{mi} - \bar{x}_m)^2}\,, s_r = \sqrt{\frac{1}{n}\sum_{i=1}^{n}(x_{ri} - \bar{x}_r)^2}\,, \quad (3)$$

where $x_{mi} = X_{mi} - X_{si}$, $x_{ri} = X_{ri} - X_{si}$; X_{mi} represents the LV2 product values, X_{ri} represents the retrieval results from the new model, and X_{si} is the reference truth (radiosonde observation or ERA5 data). Here, n is the sample size, with $i = 1,2,3,\ldots,n$. This evaluation framework enables a direct comparison of the two retrieval approaches (OE and DNN) against both the reference truth and the operational product, thereby quantifying the relative improvement achieved by the proposed methods.

(1) Clear-sky retrieval results

Under clear-sky conditions, multi-channel TB observations from the XH MWR were used to retrieve atmospheric temperature and humidity profiles using the OE method. Figure 5 presents a comparison of the MWR LV2 product and the OE-retrieved profiles against radiosonde measurements in 2020, in terms of MB and RMSE.

For temperature (Fig. 5a), the OE retrievals demonstrate consistently superior performance compared with the LV2 product across the full 0–10 km layer. The mean bias of OE-retrieved temperature relative to radiosonde data ranges from –0.83 K to 0.50 K, while the RMSE varies from 0.96 K to 3.56 K, increasing gradually with altitude and reaching its maximum at 10 km. For relative humidity (Fig. 5b), the OE retrievals also outperform the LV2 results across all altitudes, with mean biases between –6% and 6% and RMSE values ranging from 9% to 20%.

Further statistical analyses were conducted to quantify the differences between the retrieved profiles and radiosonde measurements across different altitude ranges, as well as to evaluate the accuracy improvement of the OE retrieval relative to the LV2 product (Table 2). Across all four altitude intervals ([0–2], [2–6], [6–10], and [0–10] km), the OE retrievals exhibit consistently higher accuracy. Over the full 0–10 km layer, the OE retrieval achieves a 35% improvement in temperature accuracy relative to LV2, with particularly notable gains of up to 40% within both the near-surface (0–2 km) and upper-tropospheric (6–10 km) layers. For relative humidity, the OE retrieval achieves a 25% accuracy improvement over the full profile, with the highest enhancement (29%) observed near the surface (0–2 km). These results confirm the robustness of the OE method under clear-sky conditions and highlight its capability to effectively reduce systematic biases in both temperature and humidity retrievals.

https://doi.org/10.5194/essd-2025-760
Preprint. Discussion started: 19 February 2026

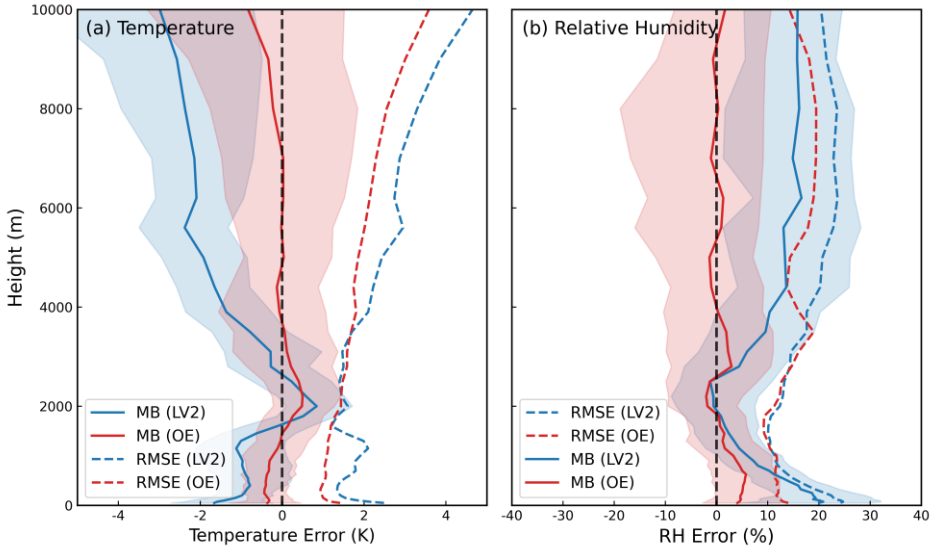

Figure 5: Vertical distributions of mean bias (MB) and root mean square error (RMSE) for LV2 and optimal estimation retrieved temperature (a) and relative humidity (b) profiles compared with radiosonde profiles in 2020. Solid lines denote the median MB, dashed lines indicate the mean MB, and shaded regions represent the interquartile range (IQR, 25–75%). A vertical dashed black line marks the zero-bias reference.

Table 2. Statistics of mean bias (MB), RMSE, and accuracy improvement rate k (%) of temperature and relative humidity profiles retrieved by LV2 and optimal estimation (OE) algorithms compared with radiosonde data across different altitude ranges.

Height (km)	Algorithms	Temperature (K)			Relative Humidity (%)		
		MB	RMSE	k (%)	MB	RMSE	Improvement rate k (%)
[0,2]	LV2	-0.93	1.68	40	11.24	16.40	29
	OE	-0.26	1.09		4.11	11.50	
[2,6]	LV2	-0.70	1.88	20	6.94	16.63	18
	OE	0.16	1.66		-1.74	14.79	
[6,10]	LV2	-2.30	3.19	42	13.31	22.87	26
	OE	-0.13	2.50		-5.32	18.98	
[0,10]	LV2	-1.02	1.91	35	10.25	17.20	25
	OE	-0.12	1.41		1.36	13.30	

(2) Cloud-sky retrieval results

Similarly, under cloudy-sky conditions, multichannel MWR TB observations at XH were used as input to the DNN-based retrieval model to obtain atmospheric temperature and humidity profiles. Figure 6 compares the DNN-retrieved profiles, the LV2 product, and radiosonde observations in 2020 in terms of MB and RMSE.

The DNN-retrieved temperature profiles exhibit markedly reduced mean biases across the entire altitude range compared to the LV2 results, with the overall mean bias remaining close to 0 K. The corresponding RMSE is significantly lower,

https://doi.org/10.5194/essd-2025-760
Preprint. Discussion started: 19 February 2026

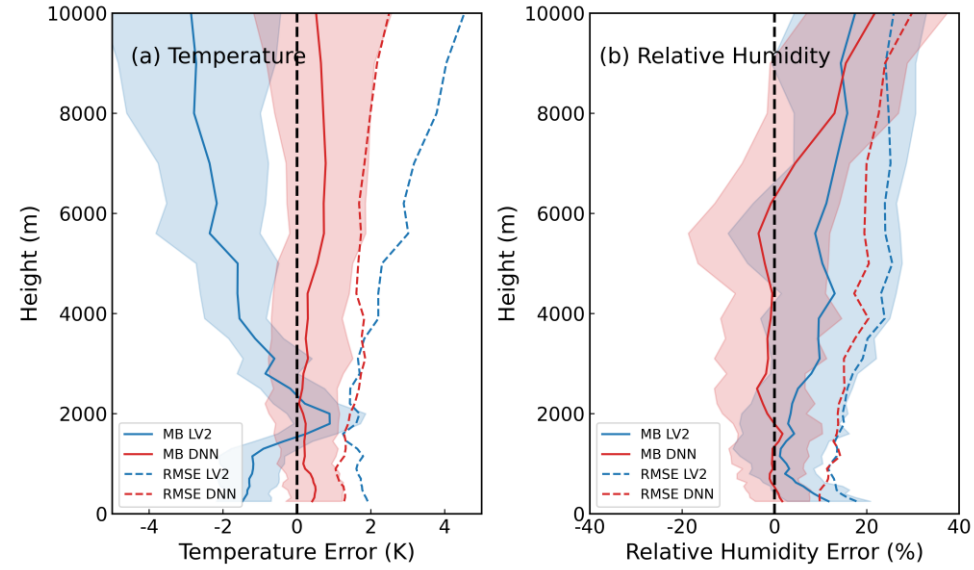

Figure 6: Same as Fig. 5, but for cloudy-sky conditions.

Table 3 summarizes the MB and RMSE values of the DNN and LV2 retrievals relative to radiosonde profiles across different altitude ranges, along with the accuracy improvement rates of the DNN retrievals. Overall, the DNN model yields systematically lower MB and RMSE values than the LV2 product across all layers, indicating clear and consistent improvement. For temperature profiles, the DNN retrieval achieves an overall 39% increase in accuracy over the 0–10 km layer relative to LV2, with the most pronounced improvements of 41% in the near-surface layer (< 2 km) and 56% in the mid-to-upper layer (6–10 km). For humidity profiles, the DNN retrieval shows a 28% overall accuracy improvement, with the highest enhancement (30%) observed in the 0–6 km range.

These findings demonstrate that the DNN model effectively captures the nonlinear relationships between TBs and atmospheric state variables under cloudy conditions, leading to a substantial reduction in retrieval errors compared with the operational LV2 product. Together, the OE and DNN results indicate that physically based and data-driven approaches can provide complementary advantages in retrieving high-quality atmospheric profiles under different sky conditions.

Table 3. Statistics of mean bias (MB), RMSE, and accuracy improvement *k* (%) of DNN and LV2 temperature and humidity profiles compared with radiosonde measurements across different altitude ranges.

Height (km)	Algorithms	Temperature (K)	Relative Humidity (%)

https://doi.org/10.5194/essd-2025-760
Preprint. Discussion started: 19 February 2026

		MB	RMSE	k	MB	RMSE	k
[0,2]	LV2	-0.96	1.67	41	4.85	13.72	29
	DNN	0.34	1.24		0.14	11.74	
[2,6]	LV2	-0.88	1.95	28	8.15	19.85	31
	DNN	0.29	1.68		-1.95	16.79	
[6,10]	LV2	-2.51	3.47	56	13.66	24.46	22
	DNN	0.72	1.92		8.04	21.54	
[0,10]	LV2	-1.14	2.02	39	7.20	17.32	28
	DNN	0.38	1.48		0.51	14.84	

4 Characteristics of the long-term and high-resolution MWR dataset

The quality-controlled, minute-level multi-channel MWR TB observations with weather classification flags were further matched with corresponding IRT, CBH, and microwave-retrieved IWV and LWP data, forming a multi-parameter dataset spanning approximately 10 years with ~1 min temporal resolution. Based on the 10-year TB dataset and the two validated retrieval models described in Section 3.3, atmospheric temperature and humidity profiles were derived from the XH MWR observations. To improve computational efficiency and meet operational requirements, the 1-minute TBs and corresponding retrievals were averaged to 10-minute intervals. The final dataset thus provides continuous, quality-controlled MWR TB observations (1-min) and derived atmospheric profiles (10-min) with enhanced retrieval accuracy, enabling systematic analyses of the temporal variability of both TBs and atmospheric profiles over the decade-long observation period.

4.1 Availability of observed brightness temperature

To clearly reflect the availability of MWR TB samples before and after quality control, Table 4 summarizes the total number of samples from 2013–2022, as well as the number and proportion of samples remaining after QC. It can be seen that data for 2013, 2014, and 2017 were relatively incomplete, primarily due to initial unfamiliarity with the instrument and delayed maintenance. Overall, except for 2017, the usable data rate of MWR TB observations over the past decade was approximately 90%, indicating good operational stability of the instrument over long-term deployment.

Table 4. Total number of observed brightness temperature samples, available samples, and their proportions from 2013 to 2022 at XH.

Year	Total Samples	Available samples	Remarks
2013	69,730	66,182 (95%)	Only April, June, July, and October
2014	176,131	165,047 (94%)	Only August–December
2015	384,168	352,415 (92%)	
2016	311,926	288,028 (92%)	

https://doi.org/10.5194/essd-2025-760
Preprint. Discussion started: 19 February 2026

2017	100,711	84,307 (84%)	Only January–March and September–December
2018	275,614	245,996 (89%)	
2019	329,943	294,954 (89%)	
2020	358,150	323,696 (90%)	
2021	433,120	394,139 (91%)	
2022	421,188	374,055 (89%)	

Figure 7 further illustrates the distribution of the comprehensive identifier *nflag* for ground-based MWR data at XH (0 = clear sky; 1 = cloudy; 2 = precipitation; 3 = uncertain samples). First, in 2013, half of the observations were concentrated in June and July, resulting in a noticeably lower frequency of clear-sky conditions compared to other years, while the proportions of cloudy and precipitation conditions were relatively higher, particularly the precipitation frequency, which was significantly above that of other years. Second, excluding 2013, the frequency of clear-sky occurrences at XH has shown a gradual decline in recent years, especially from 2018 to 2021, when the clear-sky frequency dropped to below 50%, with the corresponding frequency of cloudy conditions increasing to around 40%. The occurrence of precipitation, except for the anomalously high value in 2013, remained relatively stable in other years, generally around 5%. In addition, uncertain samples have been consistently controlled at about 10%, except in 2017, where it approached 20%, likely due to insufficient instrument maintenance or supervision.

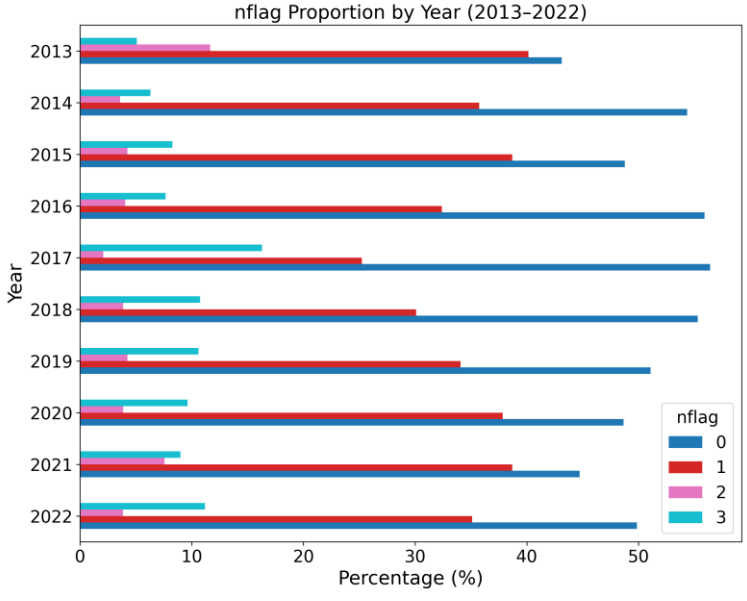

Figure 7: Distribution of the comprehensive identifier *nflag* (0: Clear-sky；1: Cloudy；2: Precipitation；3: uncertain) for ground-based MWR data at XH (2013–2022).

https://doi.org/10.5194/essd-2025-760
Preprint. Discussion started: 19 February 2026

4.2 The long-term variation trend of the high-resolution atmospheric profiles

Firstly, we examined the interannual variations of retrieved atmospheric temperature profiles, focusing on the annual mean temperature under clear-sky conditions at low altitudes (100 m, 550 m, and 1000 m) from 2013 to 2022 (Fig. 8). Linear trends of the annual mean temperature were estimated using Sen's slope, a robust non-parametric method. During the past decade, near-surface temperatures at 100 m generally ranged between 8 °C and 16 °C, with relatively higher values observed in 2019 and lower values in 2014. Similar interannual variability was evident at 550 m and 1000 m. All three elevation levels exhibited a weak but statistically significant upward trend in annual mean temperature over the study period, with warming rates of +3.70 °C dec^{-1} at 100 m, +1.89 °C dec^{-1} at 550 m, and +2.09 °C dec^{-1} at 1000 m (Fig. 8). This persistent warming across multiple altitudes suggests that the thermal changes are not confined to the immediate surface layer but extend throughout the lower boundary layer. The observed warming may reflect a combination of regional climate change signals and local anthropogenic influences, such as land-use modifications and urbanization around the XH site.

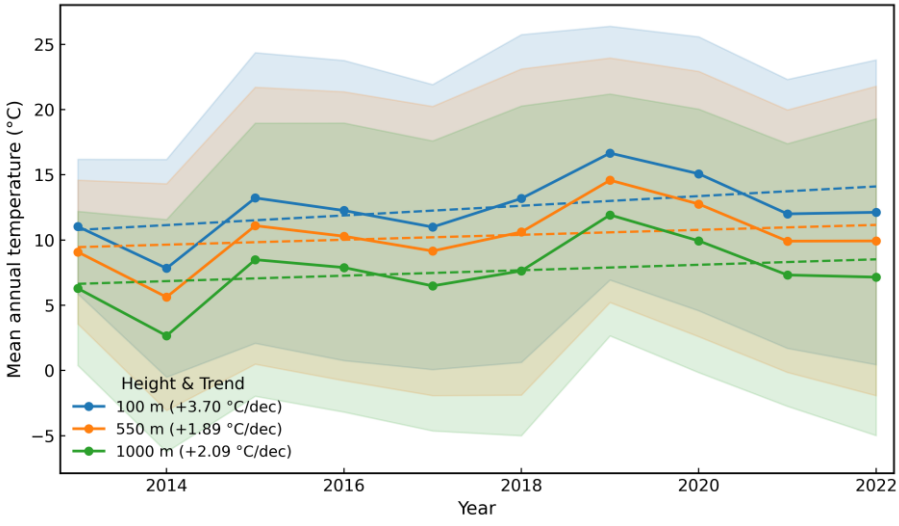

Figure 8: Annual mean temperature at three heights (100 m, 550 m, 1000 m) at XH during 2013–2022. Colored circles and lines indicate the yearly mean values, with shaded areas representing ±1 standard deviation. Dashed lines show the linear trends estimated using Sen's slope, a robust non-parametric method. Trend values (°C/decade) are indicated in the legend for each height.

The seasonal diurnal variations of temperature and relative humidity at XH during 2013–2022 reveal distinct vertical and temporal structures across the atmospheric column up to 4000 m, as illustrated in Fig. 9. The upper panels depict temperature profiles, while the lower panels show relative humidity distributions, both averaged hourly in local standard time (LST, UTC+8). Temperature exhibits a pronounced diurnal cycle near the surface, with maximum values typically occurring in the late afternoon (around 14–16 LST) and minimum values near sunrise (approximately 6 LST). This pattern reflects strong solar heating during daytime and radiative cooling at night. The surface warming is most intense in summer, when temperatures exceed 20 °C, whereas winter shows significantly lower surface temperatures and a more stable thermal stratification aloft. A clear lapse rate is observed throughout the day, with the steepest near-surface gradients developing during daytime due to

https://doi.org/10.5194/essd-2025-760
Preprint. Discussion started: 19 February 2026

convective mixing and surface heat fluxes. In contrast, nighttime inversion layers form, especially during autumn and winter, indicating reduced turbulent exchange and enhanced stability.

Relative humidity displays an inverse diurnal trend compared to temperature, peaking near sunrise and reaching its minimum in the afternoon. This behavior results from the combined effects of surface evaporation during the night and strong daytime mixing that dilutes moisture content. RH decreases rapidly with height, particularly in summer, consistent with deep convective boundary layer development and efficient vertical transport of dry air. During winter, RH profiles are more uniform vertically, with smaller gradients, reflecting weaker turbulence and limited surface moisture availability. Additionally, higher RH values persist near the surface during winter, likely due to reduced evaporation and stronger nocturnal radiation cooling.

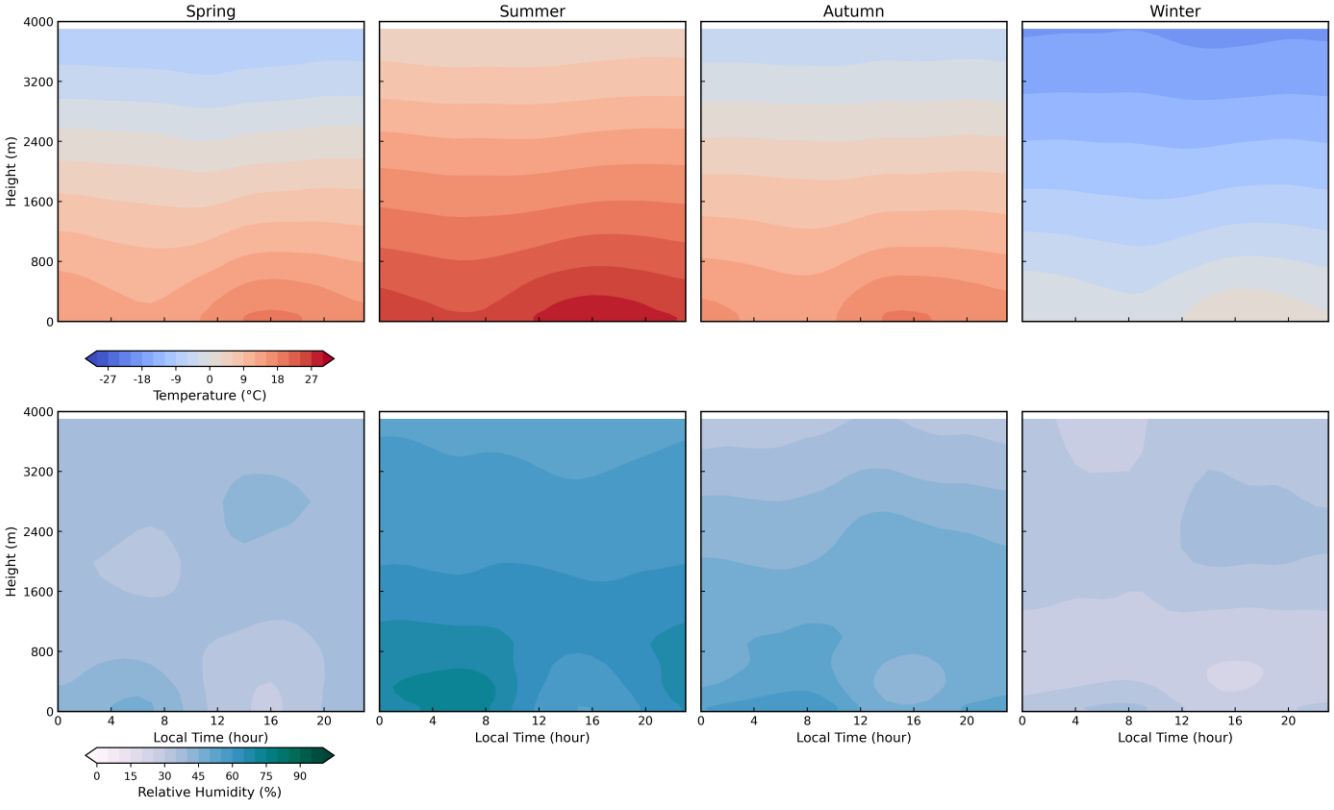

Figure 9: Seasonal diurnal variations of temperature and relative humidity at XH during 2013–2022. Upper panels show temperature profiles (°C) and lower panels show relative humidity profiles (%). Data are averaged by hour in local standard time (LST, UTC+8). Contour shading indicates the mean diurnal evolution at each vertical level, with height restricted to 0-4000 m. Colour bars at the bottom correspond to the respective variables. Seasonal panels are arranged from spring (March–May), summer (June–August), autumn (September–November) to winter (December–February).

4.3 Distribution characteristics of temperature inversions in atmospheric boundary layer

With the availability of high-temporal-resolution (10-min) temperature and humidity profiles, various atmospheric boundary layer studies can be conducted — for instance, the identification and analysis of temperature inversions. Temperature inversions include surface-based inversions (SBI) that occur near the ground, elevated inversions (EI) that form aloft, and

https://doi.org/10.5194/essd-2025-760
Preprint. Discussion started: 19 February 2026

occasionally multiple-layer inversions (Guo et al., 2020). In this study, inversion layers were automatically identified based on the vertical temperature gradient.

For each detected inversion, key characteristics such as inversion frequency, base and top height, and layer thickness were computed. For SBI, each occurrence was counted individually, whereas multiple EI layers within the same time step (Li et al., 2019) were counted only once. The temperature difference across the inversion layer represents its strength, while the inversion intensity was further derived following Zhou et al., (2024) as the ratio of temperature difference to inversion thickness (°C m^{-1}).

Figure 10 presents the monthly variations in (a) inversion frequency, (b) inversion depth, (c) inversion strength (ΔT), and (d) inversion top height for SBI and EI from 2013 to 2022, with error bars indicating one standard deviation. Both SBI and EI show distinct seasonal characteristics, with lower frequencies in spring and summer and higher frequencies in autumn and winter. The monthly variation of SBI frequency is more pronounced, reaching up to about 0.68 during autumn–winter and dropping to around 0.06 in summer, whereas EI remains relatively stable throughout the year with frequencies generally below 0.2. The inversion depth of EI remains nearly constant at around 200 m across all months, while SBI exhibits a thicker layer in spring and summer, up to approximately 300 m, possibly due to enhanced near-surface turbulence and convective mixing under warmer conditions. Regarding inversion strength (ΔT), SBI shows the highest temperature difference in summer (up to 0.9 °C), consistent with its greater depth, while winter SBI events also exhibit large temperature gradients, likely associated with strong nocturnal radiative cooling and pollutant accumulation near the surface. In terms of inversion intensity (ΔT/Depth), SBI exhibits stronger temperature gradients in winter, with peak values around 0.006 °C/m. The winter enhancement is likely linked to strong radiative cooling and pollutant accumulation near the surface.

https://doi.org/10.5194/essd-2025-760
Preprint. Discussion started: 19 February 2026

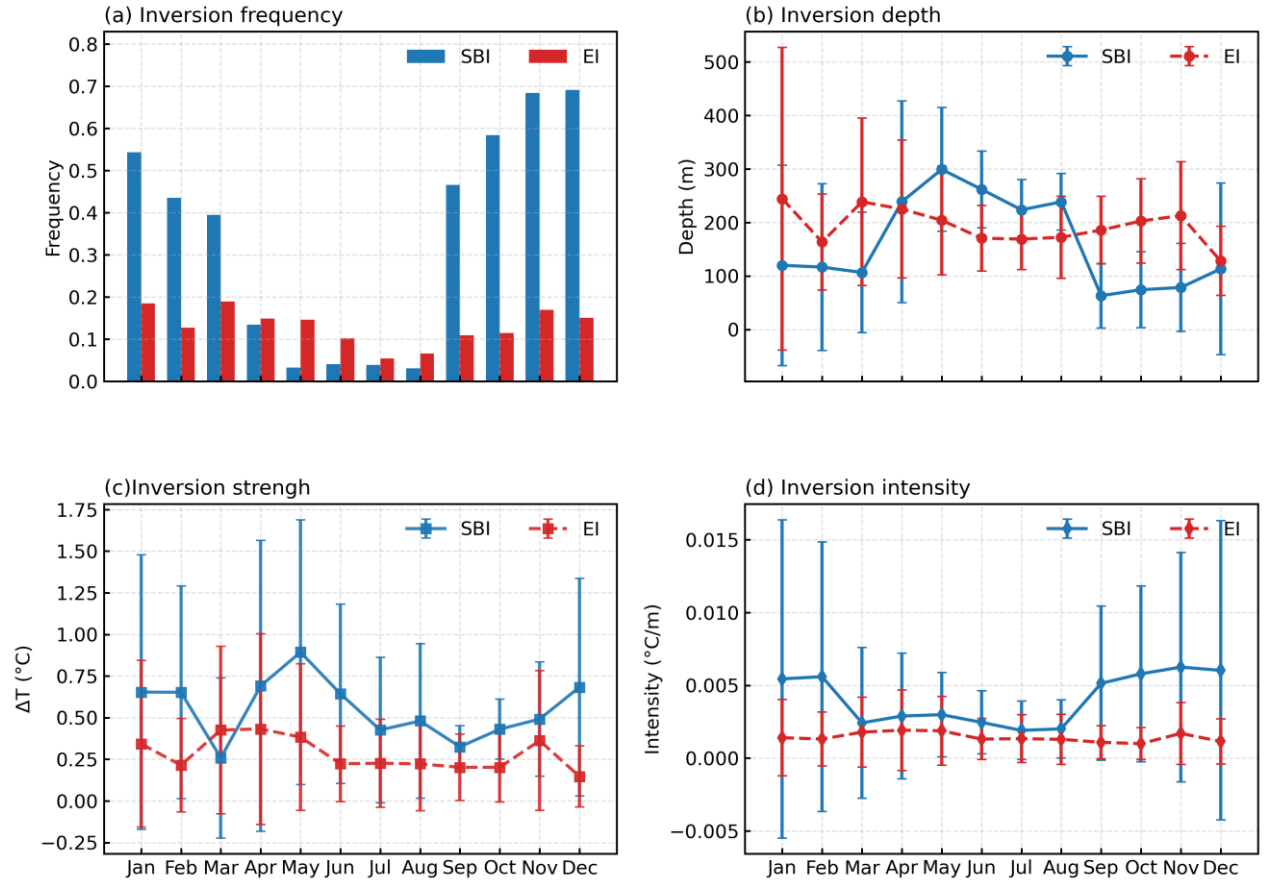

Figure 10: Monthly variations in (a) inversion frequency, (b) inversion depth, (c) temperature strength (ΔT), and (d) inversion intensity (ΔT/depth) for surface-based inversions (SBI) and elevated inversions (EI) from 2013 to 2022. The error bars denote one standard deviation.

To investigate how atmospheric inversions influence air pollution, inversion characteristics were analyzed using ground-based temperature profiles at XH during 2018–2019, combined with hourly $PM_{2.5}$ observations.

For each inversion record, the nearest hourly $PM_{2.5}$ measurement was assigned by rounding the inversion time to the closest hour. Figure 11 summarizes inversion characteristics across six $PM_{2.5}$ bins (0–35, 35–75, 75–115, 115–150, 150–250, and 250–500 μg m^{-3}).

As shown in Fig. 11a, the frequency of SBI increases with $PM_{2.5}$, reaching a maximum under the most polluted conditions, reflecting the role of SBI in trapping pollutants near the surface. Elevated inversions (EI), in contrast, exhibit a moderate peak at intermediate $PM_{2.5}$ levels (115–150 μg m^{-3}) but decrease under the highest $PM_{2.5}$ concentrations, indicating that EI contributes less to near-surface pollution accumulation during extreme pollution episodes. SBI depth gradually increases with $PM_{2.5}$, whereas EI depth is generally larger but slightly decreases under severe pollution (Fig. 11b). Similarly, SBI temperature strength and inversion intensity increase with $PM_{2.5}$ (Fig. 11c, d), highlighting stronger and more pronounced near-surface inversions that inhibit vertical mixing and favor pollutant accumulation. Conversely, EI exhibits relatively weaker ΔT and

https://doi.org/10.5194/essd-2025-760
Preprint. Discussion started: 19 February 2026

lower intensity, with a decline under extreme $PM_{2.5}$ conditions, suggesting a limited impact on surface air quality. Overall, these results indicate that the formation and strengthening of surface-based inversions directly enhance $PM_{2.5}$ accumulation near the surface, while elevated inversions are less effective in influencing surface pollution.

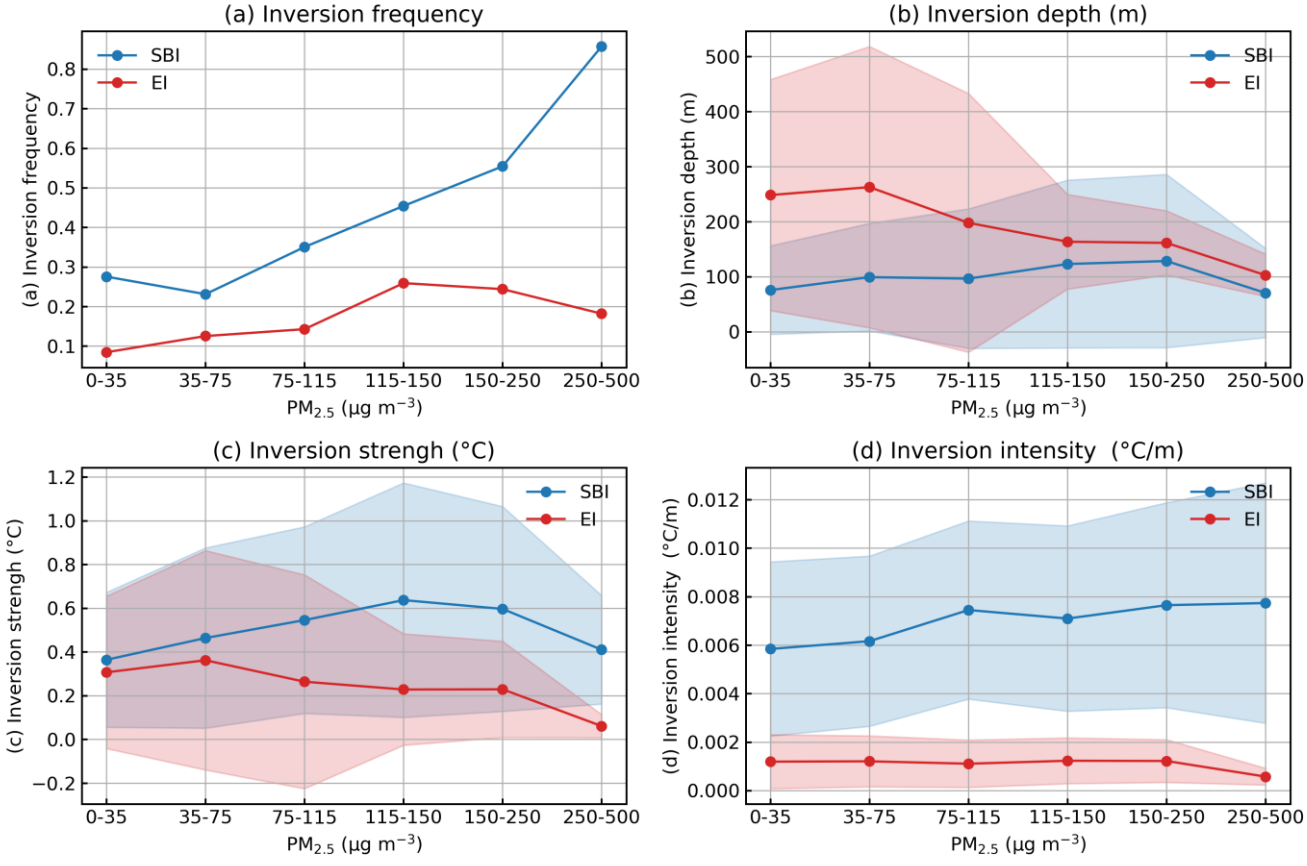

Figure 11: Statistics of inversion characteristics across different $PM_{2.5}$ concentration bins at XH during 2018-2019. Panels show (a) inversion frequency, (b) inversion depth, (c) temperature strength (ΔT), and (d) inversion intensity (ΔT/depth) for surface-based inversions (SBI, blue) and elevated temperature inversion (EI, red). Error bands indicate ±1 standard deviation.

5 Data availability

The data presented in this study are available here: https://doi.org/10.5281/zenodo.17925499 (Gong et al., 2025). This dataset consists of continuous ground-based MWR observations and corresponding retrieved atmospheric temperature and humidity profiles collected at the Xianghe site from 2013 to 2022. The quality-controlled and weather-classified brightness temperature dataset has a temporal resolution of 1 minute, covering all 14 radiometric channels of the MWR. Each record includes quality control flags and weather classification identifiers to ensure data reliability and facilitate condition-dependent analyses. The atmospheric temperature and humidity profiles were derived from the brightness temperature observations based on the

https://doi.org/10.5194/essd-2025-760
Preprint. Discussion started: 19 February 2026

validated retrieval models. To improve computational efficiency and meet operational application requirements, the retrievals are performed on 10-minute averaged brightness temperature data, resulting in a 10-minute interval profile dataset. The retrieved profiles extend from the surface up to 10 km, providing long-term, high-quality atmospheric structure information suitable for climatological analysis, model validation, and algorithm development.

6 Conclusions

Based on ground-based microwave radiometer (MWR) observations at XH from 2013 to 2022, a systematic study of brightness temperature (TB) quality control, classification, and evaluation was conducted, resulting in the construction of a long-term observational TB dataset. Using the observational TBs, radiosonde profiles, and ERA5 reanalysis data, two atmospheric temperature and humidity profile retrieval models were developed for clear-sky and cloudy-sky conditions: one based on the optimal estimation (OE) algorithm and the other on a deep neural network (DNN). The main conclusions are as follows:

(1) Comparison between observed and simulated TBs from 2013 to 2022 shows that all channels exhibit correlation coefficients above 0.97, indicating good consistency. This demonstrates the reliability of the ten-year MWR observations and the stable performance of the instrument, providing a robust basis for constructing a long-term dataset.

(2) Under clear-sky conditions, the OE retrieval outperforms the corresponding LV2 product within 10 km for both temperature and humidity profiles. The overall accuracy improvements relative to LV2 are 35 % for temperature and 25 % for relative humidity, with the largest gains observed in the near-surface layer (< 2 km), reaching 40 % and 29 %, respectively. Under cloudy-sky conditions, DNN retrievals show smaller mean bias and RMSE than LV2 below 9 km, with overall accuracy improvements of 39 % for temperature and 28 % for relative humidity across the full layer.

(3) The long-term, high-temporal-resolution (10-min) temperature and humidity profiles (2013–2022) reveal a weak but consistent near-surface warming trend across 100–1000 m. They also capture pronounced diurnal cycles—surface temperatures peak at 14–16 LST (exceeding 20 °C in summer) and RH minima occur simultaneously, along with frequent surface-based inversions (SBI), whose frequency rises from ~0.06 in summer to ~0.68 in winter. Critically, SBI occurrence increases with $PM_{2.5}$ levels, reaching >60% under severe pollution (>250 $\mu g\ m^{-3}$), demonstrating the dataset's value for boundary layer studies, climate trend analysis, and air quality forecasting.

Author contributions. YG and DF retrieval the temperature and humidity dataset and performed numerical analyses. WH and DF designed the dataset and organized the manuscript. XX conceived the idea and WN collected the samples. YG, HW and DF prepared the figures and tables. All authors discussed the results and contributed to the final paper.

Competing interests. The authors declare no competing interests.

https://doi.org/10.5194/essd-2025-760
Preprint. Discussion started: 19 February 2026

Acknowledgements. We thank the observers and technical staff, especially Qun Cheng and Qing Yao, at the Xianghe Atmospheric Observatory for their long-term microwave radiometer observations and data maintenance, and the European Centre for Medium-Range Weather Forecasts (ECMWF) for providing the ERA5 reanalysis data, and the Beijing Meteorological Observatory (station 54511) for providing the radiosonde data. Their dedicated work and data support are greatly appreciated.

Financial support. This research has been supported by the National Key Research and Development Program of China (Grant 2022YFF0801301, 2017YFC1501700), the Innovation Foundation of CPML/CMA (Grant 2023CPML-A01), the State Key Laboratory of Atmospheric Environment and Extreme Meteorology(2024QN11), the Strategic Priority Research Program of the Chinese Academy of Sciences (XDB0760402), Open Funding of the Key Laboratory of Urban Meteorology, China Meteorological Administration (LUM-2024-06).

References

Bedoya-Velásquez, A. E., Navas-Guzmán, F., De Arruda Moreira, G., Román, R., Cazorla, A., Ortiz-Amezcua, P., Benavent-Oltra, J. A., Alados-Arboledas, L., Olmo-Reyes, F. J., Foyo-Moreno, I., Montilla-Rosero, E., Hoyos, C. D., and Guerrero-Rascado, J. L.: Seasonal analysis of the atmosphere during five years by using microwave radiometry over a mid-latitude site, Atmos. Res., 218, 78–89, https://doi.org/10.1016/j.atmosres.2018.11.014, 2019.

Cimini, D., Nelson, M., Güldner, J., and Ware, R.: Forecast indices from a ground-based microwave radiometer for operational meteorology, Atmos. Meas. Tech., 8, 315–333, https://doi.org/10.5194/amt-8-315-2015, 2015.

Cimini, D., Haeffelin, M., Kotthaus, S., Löhnert, U., Martinet, P., O'Connor, E., Walden, C., Coen, M. C., and Preissler, J.: Towards the profiling of the atmospheric boundary layer at European scale—introducing the COST Action PROBE, Bull. Atmos. Sci. Technol., 1, 23–42, https://doi.org/10.1007/s42865-020-00003-8, 2020.

De Angelis, F., Cimini, D., Löhnert, U., Caumont, O., Haefele, A., Pospichal, B., Martinet, P., Navas-Guzmán, F., Klein-Baltink, H., Dupont, J.-C., and Hocking, J.: Long-term observations minus background monitoring of ground-based brightness temperatures from a microwave radiometer network, Atmos. Meas. Tech., 10, 3947–3961, https://doi.org/10.5194/amt-10-3947-2017, 2017.

Fu X. and Tan J.: Quality control of temperature and humidity profile retrievals from ground-based microwave radiometer, Journal of Applied Meteorological Science, 28, 209, 2017.

Gong, Y., He, W., Fu, D., Xia, X., Shi, H., Nan, W., Wang, P., and Chen, H.: The first decadal-scale ground-based microwave radiometer dataset in China: Brightness temperature and thermodynamic profiles from Xianghe (2013–2022), Zenodo [data set], https://doi.org/10.5281/zenodo.17925499, 2025.

Guo, J., Chen, X., Su, T., Liu, L., Zheng, Y., Chen, D., Li, J., Xu, H., Lv, Y., He, B., Li, Y., Hu, X.-M., Ding, A., and Zhai, P.: The climatology of lower tropospheric temperature inversions in China from radiosonde measurements: roles of black carbon, local meteorology, and large-scale subsidence, J. Clim., 33, 9327–9350, https://doi.org/10.1175/JCLI-D-19-0278.1, 2020.

https://doi.org/10.5194/essd-2025-760
Preprint. Discussion started: 19 February 2026

Guo, Y., Du, L., and Lyu, G.: SAR target detection based on domain adaptive faster R-CNN with small training data size, Remote Sens., 13, 4202, https://doi.org/10.3390/rs13214202, 2021.

He, M., Wang, D., Ding, W., Wan, Y., Chen, Y., and Zhang, Y.: A validation of Fengyun4A temperature and humidity profile products by radiosonde observations, Remote Sens., 11, 2039, https://doi.org/10.3390/rs11172039, 2019.

He, W., Cheng, Y., Zou, R., Wang, P., Chen, H., Li, J., and Xia, X.: Radiative transfer model simulations for ground-based microwave radiometers in north China, Remote Sens., 13, 5161, https://doi.org/10.3390/rs13245161, 2021.

Hersbach, H., Bell, B., Berrisford, P., Hirahara, S., Horányi, A., Muñoz-Sabater, J., Nicolas, J., Peubey, C., Radu, R., Schepers, D., Simmons, A., Soci, C., Abdalla, S., Abellan, X., Balsamo, G., Bechtold, P., Biavati, G., Bidlot, J., Bonavita, M., De Chiara, G., Dahlgren, P., Dee, D., Diamantakis, M., Dragani, R., Flemming, J., Forbes, R., Fuentes, M., Geer, A., Haimberger, L., Healy, S., Hogan, R. J., Hólm, E., Janisková, M., Keeley, S., Laloyaux, P., Lopez, P., Lupu, C., Radnoti, G., De Rosnay, P., Rozum, I., Vamborg, F., Villaume, S., and Thépaut, J.: The ERA5 global reanalysis, Q. J. R. Meteorol. Soc., 146, 1999–2049, https://doi.org/10.1002/qj.3803, 2020.

Hewison, T. J.: 1D-VAR retrieval of temperature and humidity profiles from a ground-based microwave radiometer, IEEE Trans. Geosci. Remote Sens., 45, 2163–2168, https://doi.org/10.1109/tgrs.2007.898091, 2007.

Hou, X., Han, Y., Hu, X., and Weng, F.: Verification of Fengyun-3D MWTS and MWHS Calibration Accuracy Using GPS Radio Occultation Data, J. Meteorol. Res., 33, 695–704, https://doi.org/10.1007/s13351-019-8208-9, 2019.

Huang Z., Xu G., Wang X., and Tang Y.: Applications of Ground-based Microwave Radiation Data to Short-term Rainstorm and Potential Forecast, J Appl Meteor Sci, 24, 576–584, 2013.

Lai, Y., Li, L., Wang, H., Zhang, H., Xia, Y., Wei, T., and Meng, L.: Variation Characteristics and Influencing Factors of Atmospheric Convective Boundary Layer Height over Beijing Region in the Past 30 Years, Meteorological Monthly, 50, 1417–1428, https://doi.org/10.7519/j.issn.1000-0526.2024.080101, 2024.

Li, J., Chen, H., Li, Z., Wang, P., Fan, X., He, W., and Zhang, J.: Analysis of low-level temperature inversions and their effects on aerosols in the lower atmosphere, Adv. Atmos. Sci., 36, 1235–1250, https://doi.org/10.1007/s00376-019-9018-9, 2019.

Liu, G.: A fast and accurate model for microwave radiance calculations, J. Meteorol. Soc. Jpn., II, 76, 335–343, https://doi.org/10.2151/jmsj1965.76.2_335, 1998.

Liu, Y., Chen, X., Ma, Y., Cao, D., Sun, F., Xu, X., and Zhang, Q.: Application of ground-based microwave radiometers to optimize the estimation method of cloud liquid water on the Tibetan Plateau, ADVANCES IN ATMOSPHERIC SCIENCES, https://doi.org/10.1007/s00376-025-4416-7, 2025.

Löhnert, U. and Maier, O.: Operational profiling of temperature using ground-based microwave radiometry at Payerne: prospects and challenges, Atmos. Meas. Tech., 5, 1121–1134, https://doi.org/10.5194/amt-5-1121-2012, 2012.

Maahn, M., Turner, D. D., Löhnert, U., Posselt, D. J., Ebell, K., Mace, G. G., and Comstock, J. M.: Optimal estimation retrievals and their uncertainties, Bull. Am. Meteorol. Soc., 101, E1512–E1523, https://doi.org/10.1175/BAMS-D-19-0027.1, 2020.

Madhulatha, A., Rajeevan, M., Venkat Ratnam, M., Bhate, J., and Naidu, C. V.: Nowcasting severe convective activity over southeast India using ground-based microwave radiometer observations, J. Geophys. Res.: Atmos., 118, 1–13, https://doi.org/10.1029/2012JD018174, 2013.

https://doi.org/10.5194/essd-2025-760
Preprint. Discussion started: 19 February 2026

Malmgren-Hansen, D., Laparra, V., Aasbjerg Nielsen, A., and Camps-Valls, G.: Statistical retrieval of atmospheric profiles with deep convolutional neural networks, ISPRS J. Photogramm. Remote Sens., 158, 231–240, https://doi.org/10.1016/j.isprsjprs.2019.10.002, 2019.

Martinet, P., Dabas, A., Donier, J.-M., Douffet, T., Garrouste, O., and Guillot, R.: 1D-Var temperature retrievals from microwave radiometer and convective scale model, Tellus A: Dyn. Meteorol. Oceanogr., 67, 27925, https://doi.org/10.3402/tellusa.v67.27925, 2015.

Navas-Guzmán, F., Kämpfer, N., and Haefele, A.: Validation of brightness and physical temperature from two scanningmicrowave radiometers in the 60 GHz O_2 band using radiosonde measurements, Atmos. Meas. Tech., 9, 4587–4600, https://doi.org/10.5194/amt-9-4587-2016, 2016.

Rodgers, C. D.: Inverse methods for atmospheric sounding: theory and practice, World Scientific, Singapore ; [River Edge, N.J.], 240 pp., 2000.

Rüfenacht, R., Haefele, A., Pospichal, B., Cimini, D., Bircher-Adrot, S., Turp, M., and Sugier, J.: EUMETNET opens to microwave radiometers for operational thermodynamical profiling in Europe, Bull. Atmos. Sci. Technol., 2, 4, s42865-021-00033-w, https://doi.org/10.1007/s42865-021-00033-w, 2021.

Temimi, M., Fonseca, R. M., Nelli, N. R., Valappil, V. K., Weston, M. J., Thota, M. S., Wehbe, Y., and Yousef, L.: On the analysis of ground-based microwave radiometer data during fog conditions, Atmos. Res., 231, 104652, https://doi.org/10.1016/j.atmosres.2019.104652, 2020.

Trent, T., Siddans, R., Kerridge, B., Schröder, M., Scott, N. A., and Remedios, J.: Evaluation of tropospheric water vapour and temperature profiles retrieved from MetOp-a by the infrared and microwave sounding scheme, Atmos. Meas. Tech., 16, 1503–1526, https://doi.org/10.5194/amt-16-1503-2023, 2023.

Turner, D. D., Clough, S. A., Liljegren, J. C., Clothiaux, E. E., Cady-Pereira, K. E., and Gaustad, K. L.: Retrieving Liquid Wat0er Path and Precipitable Water Vapor From the Atmospheric Radiation Measurement (ARM) Microwave Radiometers, IEEE Trans. Geosci. Remote Sensing, 45, 3680–3690, https://doi.org/10.1109/TGRS.2007.903703, 2007.

Wei, J., Shi, Y., Ren, Y., Li, Q., Qiao, Z., Cao, J., Ayantobo, O. O., Yin, J., and Wang, G.: Application of Ground-Based Microwave Radiometer in Retrieving Meteorological Characteristics of Tibet Plateau, Remote Sens., 13, 2527, https://doi.org/10.3390/rs13132527, 2021.

Xin, J., Wang, Y., Pan, Y., Ji, D., Liu, Z., Wen, T., Wang, Y., Li, X., Sun, Y., Sun, J., Wang, P., Wang, G., Wang, X., Cong, Z., Song, T., Hu, B., Wang, L., Tang, G., Gao, W., Guo, Y., Miao, H., Tian, S., and Wang, L.: The Campaign on Atmospheric Aerosol Research Network of China: CARE-China, Bull. Am. Meteorol. Soc., 96, 1137–1155, https://doi.org/10.1175/BAMS-D-14-00039.1, 2015.

Xu, G.: A Review of Remote Sensing of Atmospheric Profiles and Cloud Properties by Ground-Based Microwave Radiometers in Central China, Remote Sens., 16, 966, https://doi.org/10.3390/rs16060966, 2024.

Yan, X., Liang, C., Jiang, Y., Luo, N., Zang, Z., and Li, Z.: A Deep Learning Approach to Improve the Retrieval of Temperature and Humidity Profiles From a Ground-Based Microwave Radiometer, IEEE Trans. Geosci. Remote Sens., 58, 8427–8437, https://doi.org/10.1109/TGRS.2020.2987896, 2020.

Zhang, L., Liu, M., He, W., Xia, X., Yu, H., Li, S., and Li, J.: Ground passive microwave remote sensing of atmospheric profiles using WRF simulations and machine learning techniques, J. Meteorol. Res., 38, 680–692, https://doi.org/10.1007/s13351-024-4004-2, 2024.

https://doi.org/10.5194/essd-2025-760
Preprint. Discussion started: 19 February 2026

Zhang, X., Wang, Z., Mao, J., Wang, Z., Zhang, D., and Tao, F.: Experiments on improving temperature and humidity profile retrieval for ground-based microwave radiometer, J Appl Meteor Sci, 31, 385–396, https://doi.org/10.11898/1001-7313.20200401, 2020.

Zhao, Y., Zhou, D., and Yan, H.: An improved retrieval method of atmospheric parameter profiles based on the BP neural network, Atmos. Res., 213, 389–397, https://doi.org/10.1016/j.atmosres.2018.06.025, 2018.

Zhou, X., Zhang, C., Li, Y., Sun, J., Chen, Z., and Li, L.: Concurrence of Temperature and Humidity Inversions in Winter in Qingdao, China, Geophys. Res. Lett., 51, e2024GL108350, https://doi.org/10.1029/2024GL108350, 2024.

Zhu, L., Bao, Y., Lu, Q., Fan, S., Petropoulos, G. P., Mao, J., Li, Y., and Li, X.: A Method for Retrieving Thermodynamic Atmospheric Profiles Using Microwave Radiometers of Meteorological Observation Networks, IEEE Trans. Geosci. Remote Sens., 60, 1–11, https://doi.org/10.1109/TGRS.2022.3208939, 2022.

Zou, R., He, W., Wang, P., Mao, J., Chen, H., Li, J., Nan, W., and Chang, Y.: Assessment of Radiative Transfer Models Based on Observed Brightness Temperature from Ground-Based Microwave Radiometer, Chinese Journal of Atmospheric Sciences, 45, 605–616, https://doi.org/10.3878/j.issn.1006-9895.2008.20134, 2021.